

Noise reduction in Hyperion high dynamic range hyperspectral data using machine learning and statistical techniques

Priyanka Nair¹, Devesh Kumar Srivastava¹, Roheet Bhatnagar²

¹Department of Information Technology, Faculty of Engineering, Manipal University Jaipur, Jaipur, India

²Department of Computer Science and Engineering, Faculty of Engineering, Manipal University Jaipur, Jaipur, India

Article Info

Article history:

Received Mar 6, 2024

Revised Jul 20, 2024

Accepted Aug 6, 2024

Keywords:

Denoising autoencoders

Hyperspectral imagery

Machine learning algorithms
for denoising

Principal component analysis

Statistical methods for
denoising

ABSTRACT

Numerous remote sensing applications rely heavily on hyperspectral imagery, but it is frequently plagued by noise, which degrades the data quality and hinders subsequent analysis. In this research paper, we present an in-depth analysis of noise removal techniques for hyperspectral imagery, specifically for data acquired from the Hyperion EO-1 sensor. Setting off with obtaining Hyperion data and the pre-processing stages, the paper discusses the acquisition and denoising of Hyperion data. The hyperspectral data considered is in the high dynamic range (HDR) format, which maintains the original imagery's complete dynamic range. The study explores various noise reduction methods, such as minimum noise fraction (MNF), principal component analysis (PCA), wavelet denoising, non-local means (NLM), and denoising autoencoders, aimed at enhancing the signal-to-noise ratio. The effectiveness of these techniques is evaluated through visual quality, mean square error (MSE), and peak signal-to-noise ratio (PSNR), alongside their impact on mineral exploration. Furthermore, the paper investigates the application of machine learning algorithms on denoised data for mineral identification, highlighting the potential of integrating denoising techniques with machine learning for improved mineral exploration. This comparative analysis aims to identify the most efficient noise removal methods for hyperspectral imagery, facilitating higher quality data for subsequent analysis.

This is an open access article under the [CC BY-SA](https://creativecommons.org/licenses/by-sa/4.0/) license.



Corresponding Author:

Devesh Kumar Srivastava

Department of Information Technology, Faculty of Engineering, Manipal University Jaipur

Jaipur, Rajasthan, India

Email: devesh.srivastava@jaipur.manipal.edu

1. INTRODUCTION

The exponential growth in remote sensing technologies has unlocked unprecedented capabilities for observing the Earth's surface. Among these technologies, hyperspectral imaging stands out for its ability to capture a wide spectrum of information across hundreds of contiguous spectral bands [1], [2]. This rich spectral resolution facilitates detailed analysis and identification of materials, making it invaluable for applications such as mineral exploration, agriculture, environmental monitoring, and military surveillance. The hyperspectral sensors can capture images in 100-250 contiguous spectral bands, each of which contains unique properties of elements on the Earth's surface thereby enabling the collecting of high-resolution data and improving the ability to differentiate between different types of materials. Because of its hyperspectral capacity, mineral prospectivity mapping and full geological studies are now much more precise [3], [4]. However, the potential of hyperspectral imagery is often compromised by the presence of noise—a pervasive issue that can significantly degrade data quality. Noise in hyperspectral images arises from various sources,

including sensor imperfections, atmospheric interference, and processing anomalies, leading to challenges in accurate data interpretation and analysis.

The challenge of noise in hyperspectral data is multifaceted, affecting both the reliability and the interpretability of the imagery [5]. Traditional noise reduction techniques, while useful, often fall short in addressing the complexity and variability of noise across different spectral bands. Moreover, these methods may inadvertently remove important spectral features or fail to adapt to the unique characteristics of each band, resulting in suboptimal denoising outcomes. Consequently, there is a critical need for advanced denoising strategies that can effectively mitigate noise while preserving the integrity and richness of hyperspectral data.

This paper introduces a comprehensive approach to denoising hyperspectral imagery, particularly focusing on data acquired from the Hyperion Earth Observation-1 (Hyperion EO-1) sensor. We propose a two-pronged strategy that combines the strengths of traditional statistical methods and cutting-edge machine learning (ML) techniques [6], specifically leveraging the capabilities of denoising autoencoders. Our approach is designed to tackle the inherent challenges of hyperspectral data denoising by i) applying statistical denoising techniques: Initial preprocessing employs techniques such as minimum noise fraction (MNF), principal component analysis (PCA), and wavelet denoising to reduce noise levels and improve data quality. These methods target different types of noise and are carefully selected based on their compatibility with the specific characteristics of hyperspectral imagery and ii) implementing machine learning-based denoising: we introduce a denoising autoencoder—a sophisticated deep learning model tailored to hyperspectral data. This model is trained to learn the intricate patterns of noise across the spectrum, enabling it to effectively filter out noise while retaining critical spectral information. The denoising autoencoder represents a significant advancement in hyperspectral image processing, offering adaptability and superior denoising performance across all bands. The primary objective of this research is to enhance the quality of hyperspectral imagery by effectively reducing noise, thereby facilitating more accurate and reliable data analysis for various applications. By integrating statistical methods with ML algorithms, we aim to offer a robust solution that addresses the limitations of conventional denoising techniques.

The application of machine learning and deep learning has been a significant trend in noise reduction for hyperspectral images. For instance, Huang *et al.* [7] and Lian *et al.* [8] have explored the use of attention-assisted convolutional neural networks (CNNs) and neural networks that combine spatial-spectral information for denoising, indicating a shift towards more sophisticated, data-driven approaches for capturing and reducing noise. Huang *et al.* [7] and Chan and Li [9] discussed spectral-spatial methods for image classification and denoising, highlighting the importance of considering both spectral and spatial dimensions of hyperspectral images for effective noise reduction. Feng *et al.* [10] and Zhu *et al.* [11] focused on image fusion techniques as a means to reduce noise and improve image quality, indicating the potential of integrating hyperspectral and multispectral imagery for enhanced performance. The works by Rani *et al.* [1] and Tagwai *et al.* [2] in the context of geological mapping and mineral exploration showcase the utility of noise-reduced hyperspectral images in identifying mineral deposits and geological features. Zhao *et al.* [12] and Deng *et al.* [13] presented methods that exploit spatial and spectral correlations within hyperspectral images for denoising, illustrating the effectiveness of integrating spatial information with spectral analysis. Yang *et al.* [14] and Xiaorui *et al.* [15] explored wavelet-based and PCA-based denoising methods, respectively, offering insights into the use of these mathematical techniques for noise reduction in hyperspectral images.

The thesis by Granek [16] at the University of British Columbia in 2016 explores the use of machine learning algorithms for mineral prospectivity mapping. It highlights the challenge of effectively managing and integrating multi-parameter datasets within fixed exploration budgets. The study introduces two novel approaches: a modified support vector machine algorithm that accounts for uncertainties in data and labels, demonstrated with a copper-gold porphyry target mapping in British Columbia, and the use of CNNs for their spatial pattern recognition capabilities, tested on a subset of the quantum excited state database (QUEST) dataset. This work has been employed as a motivation and progressive step towards incorporating advanced computational techniques in mineral exploration applied on Iron rich land surfaces in India. The study by Wang *et al.* [17] utilized HySpex airborne hyperspectral data and the random forest algorithm to identify and map alteration minerals in the Yudai porphyry Cu (Au, Mo) mineralization area in Eastern Tianshan, Northwest China. This research demonstrates that airborne hyperspectral remote sensing can provide rapid, non-destructive, and high-quality reflectance spectra. These spectra are essential for accurate mineral mapping in complex geological environments.

Future directions on the past work by research have been on the band set including the employment of sophisticated models that can better handle the high dimensionality and data volume of hyperspectral images, the exploration of unsupervised and semi-supervised learning methods for scenarios with limited labeled data, and the application of these advanced noise reduction techniques in new fields beyond those

traditionally associated with remote sensing. Our contributions are twofold employing Hyperion EO-1 sensor data: enhanced data quality: by significantly reducing noise across the hyperspectral dataset, taking individual band processing thereby improving the signal-to-noise ratio (SNR), preserving the fidelity of the original spectral signatures; advanced analytical capabilities: the improved data quality lays the groundwork for more sophisticated analyses, including material identification and classification, leading to better outcomes in mineral exploration, environmental monitoring, and other key applications. This paper details the methodology, implementation, and validation of our proposed denoising strategy, highlighting its effectiveness through quantitative metrics and qualitative assessments. Through this work, we demonstrate the potential of combining statistical and machine learning techniques to overcome the challenges of hyperspectral data denoising, paving the way for advancements in remote sensing analysis specifically in the realm of Geosciences.

2. RESEARCH FRAMEWORK

This paper presents a methodology for enhancing the quality of hyperspectral images obtained from the Hyperion EO-1 sensor by integrating conventional statistical approaches with advanced machine learning strategies for effective noise mitigation. The comprehensive procedure adopted is delineated in Figure 1, with the aspects discussed in this paper emphasized by the blue highlighted pathway. The subsequent crucial stage is endmember extraction, which identifies the purified spectra of materials present in the scene. Using the extracted endmembers, spectral unmixing is then carried out. This method estimates the fractional abundance of each endmember in each pixel, which provides valuable information about the distribution of various materials in the scene. In the preliminary phase of our framework, we prioritize the crucial process of accurately identifying mineral maps. This foundational step is paramount as it sets the groundwork for subsequent analysis and extraction strategies, ensuring precision in the identification and localization of valuable mineral deposits.

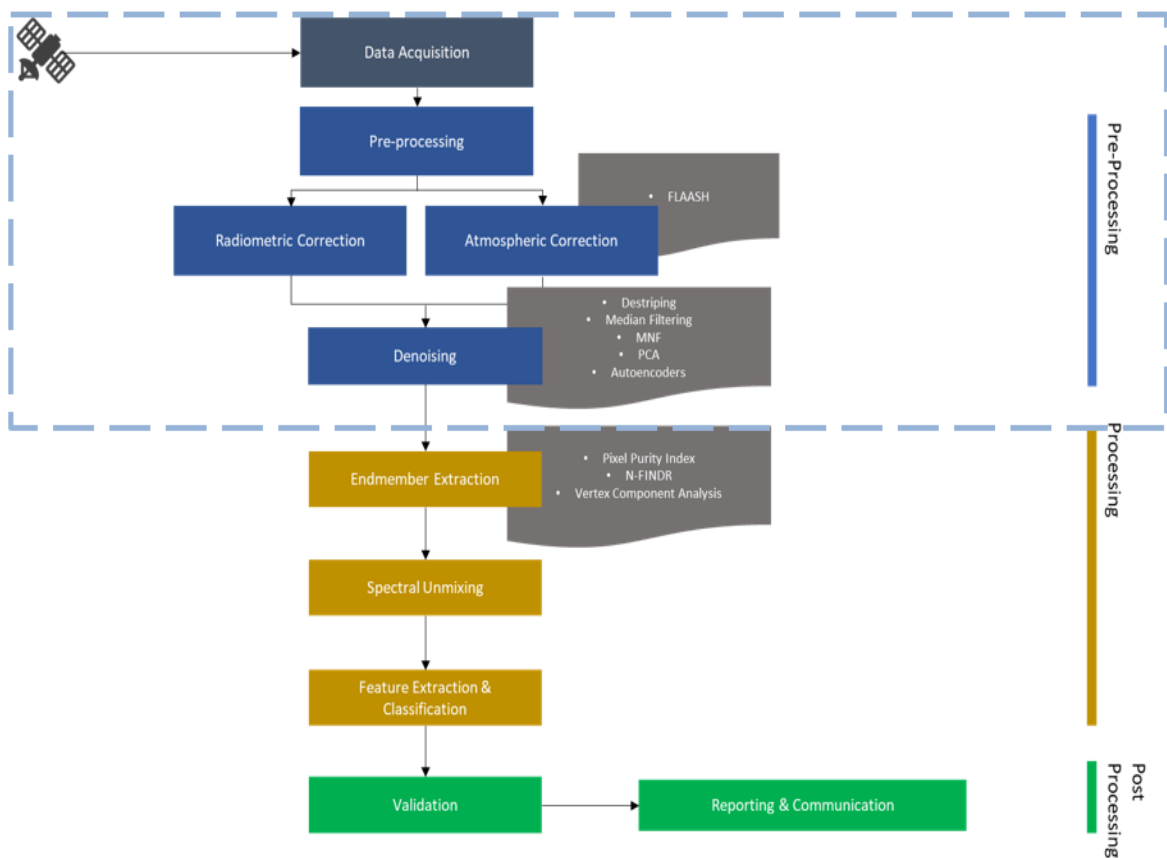


Figure 1. Research framework for mineral prospectivity mapping with stages of pre-processing, processing and post-processing

2.1. Dataset

The Level 1R (L1R) data collected by the Hyperion sensor on the Earth Observing-1 (EO-1) satellite is called the EO-1 Hyperion L1R collection. Kiriburu is being considered as a place to map minerals because of its natural importance [18]. Valuable rocks or metals have been found in the area, which makes it interesting for mapping and exploring. The data imported comprises 242 spectral bands. Each pixel corresponds to a spectral band in a particular wavelength. Figure 2 shows the area under study.

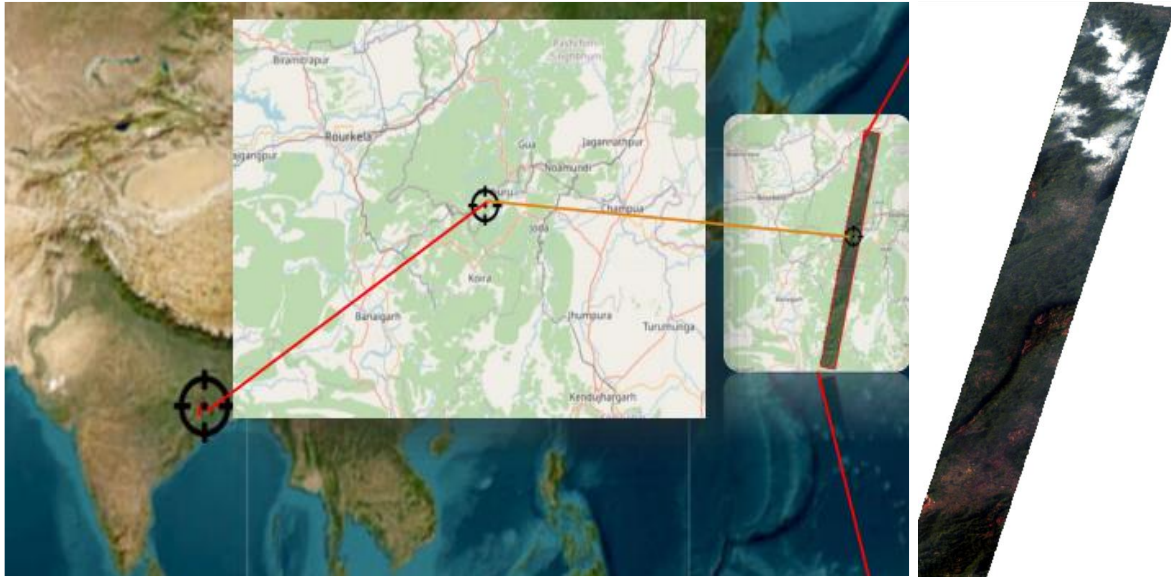


Figure 2. Kiriburu region: detailed analysis within coordinates [UL: 22.498708° N, 85.322800° E; UR: 22.486155° N, 85.393441° E; LL: 21.548074° N, 85.108266° E; LR: 21.535850° N, 85.178149° E], Bands: 242, dimensions: width 1041, height 3571, radiance scaling: VNIR 40, SWIR 80, grid cell size: 30.00

3. DATA PREPROCESSING

Remote sensing and image processing use several noise-reduction methods to improve data quality. Noise reduction methods improve data fidelity, enabling improved analysis and interpretation. These strategies improve data integrity in our research area, yielding more accurate results.

3.1. Bad band removal

As a preliminary step we will remove all bands which contain no information. The primary goal of bad band removal is to eliminate spectral bands that do not contribute useful information to the dataset. These could be bands that are excessively noisy, contain artifacts, or simply do not capture relevant spectral information due to sensor limitations or atmospheric effects [19], [20].

For each pixel across all bands, the mean or median spectral signature is calculated. This statistical analysis helps in identifying the average behavior of the spectrum across the dataset. By comparing individual pixel values in each band to the calculated mean or median, bands that significantly deviate from these central tendencies are flagged. Significant deviation indicates that the band might be noisy or contain artifacts that could interfere with accurate data analysis.

$$SNR \text{ (Signal - to - Noise Ratio) } = \frac{\text{Mean Signal} - \text{Mean Noise}}{\text{Standard Deviation of Noise}} \quad (1)$$

The higher the SNR value (calculated by (1)), the better the signal quality in that spectral band. Lower SNR values may indicate higher noise levels relative to the signal and suggest that the band may be less informative or less reliable for analysis. Of the original 242 bands, 198 bands were retained after removing those identified as bad. This reduction is based on the premise that excluding these bands will lead to a more accurate and reliable analysis, focusing on the data that most accurately represents the observed scene.

Figure 3(a) represents the mean spectral signatures across the entire hyperspectral dataset. Each band's average signal intensity is plotted, allowing for a visual assessment of which bands carry significant

information and which appear aberrant or flat (indicative of noise or lack of information). Figure 3(b) contrasts the profiles of bands considered “good” or useful for analysis against those deemed “bad” or unsuitable.

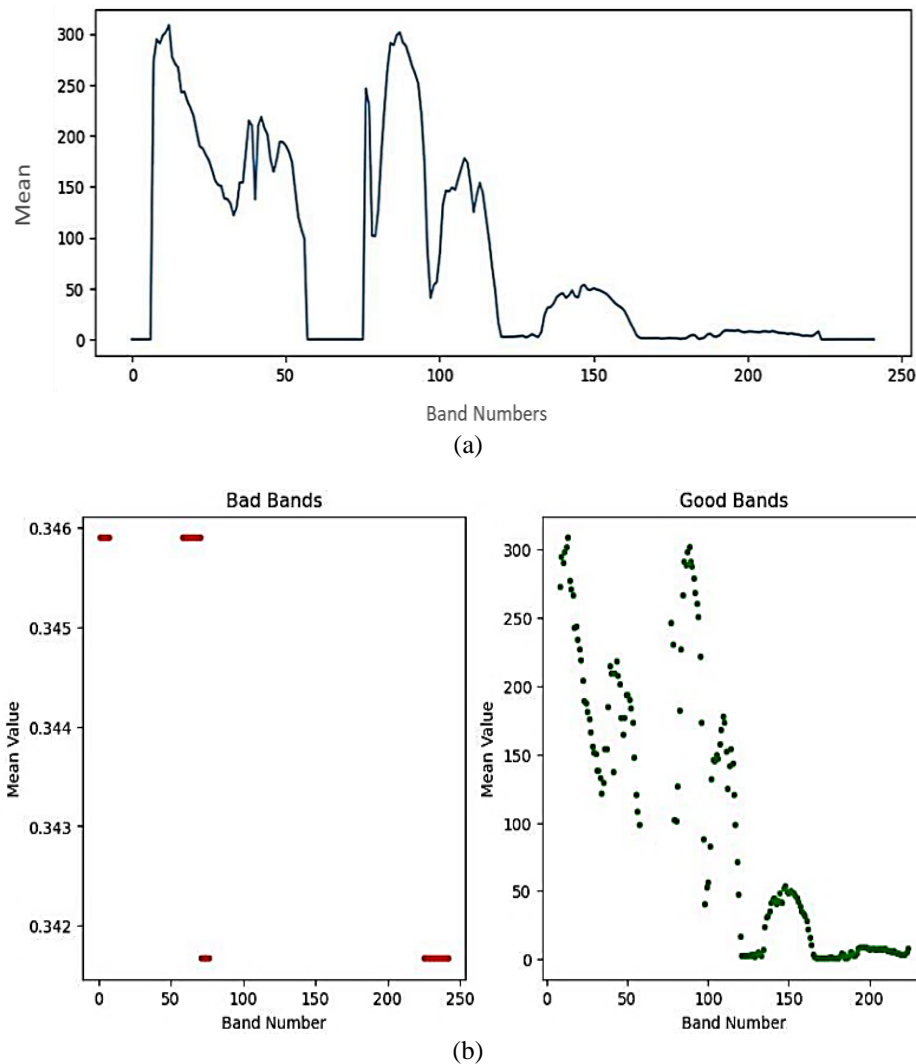


Figure 3. Bad band removal for hyperspectral imagery (HSI) dataset (a) spectral mean representation of 242 bands and (b) generated good and bad band profiles

3.2. Radiometric correction and atmospheric calibration

Despite being radiometrically corrected, the L1R EO-1 Hyperion data undergoes Level-1 processing, which includes calibration to convert the raw data numbers (DN) to at-sensor radiance values. We will employ the metadata of our area under study for radiometric calibration. Radiance conversion and reflectance conversion are carried to obtain the spectral mapping of radiometrically calibrated dataset.

As a next crucial preprocessing phase in remote sensing and satellite image analysis is atmospheric correction. The atmosphere can introduce various types of noise and distortions to the recorded signal, compromising the data's precision and interpretability. These atmospheric effects are estimated and compensated for by atmospheric correction techniques, resulting in more accurate and reliable data for further analysis [21]. For the EO-1 radiometric calibrated data we apply atmospheric correction leading to the result and correction. Figure 4 shows the atmospherically corrected EO-1 data. fast line-of-sight atmospheric analysis of spectral hypercubes (FLAASH) is an implementation within the ENVI software package, which provides an interface for performing atmospheric correction on Hyperion data. The actual equations and details of the FLAASH algorithm are proprietary to the ENVI software. The FLAASH atmospheric correction results “visibility = 25.1607 km” and “average water amount = 3.8937 cm” received, provide information about the scene's atmospheric conditions and water content.

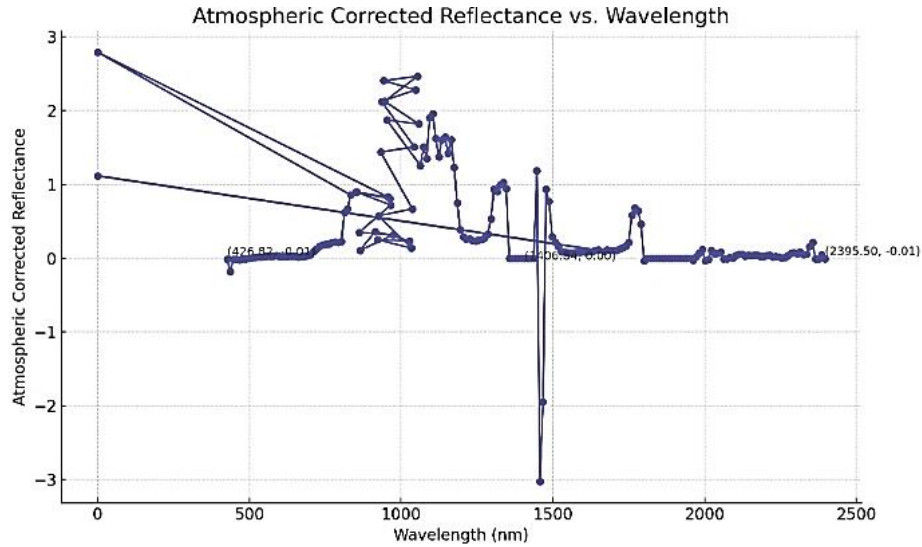


Figure 4. Spectral profiles of atmospherically corrected EO-1 data

3.3. Destriping

Destriping is a preprocessing technique employed to eliminate striping artefacts from hyperspectral images, such as those acquired by the Hyperion sensor [22]. The striping artefacts are undesirable linear patterns or bands. The destriping process attempts to correct these artefacts and enhance the image data's overall quality and precision.

It will not be sufficient to remove the stripes from the HIS on the whole but need to be removed on individual band level. Various methods, such as interpolation, filtering, and statistical modelling, can be used to estimate the values of missing or corrupted pixels. We have employed mean filtering on corrupted pixels of the band. Figure 5 shows the destriping of band 21, wherein Figure 5(a) shows the band with vertical strip presence, Figure 5(b) shows the focused view of strip, and destriped band in Figure 5(c). Similar results of destriping are derived for all 198 bands.

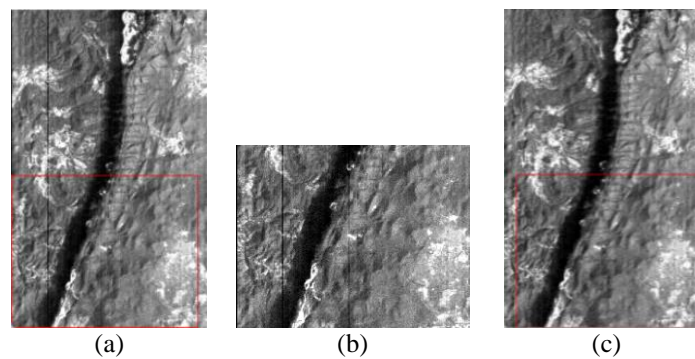


Figure 5. Destriping of band 21 of area under study (a) Figure shows the band with vertical strip presence; (b) Figure shows the zoomed in view of the stripe; and (c) Figure shows the destriping effect with the removal of vertical stripe from Band 21

3.4. Median filtering

A nonlinear filter known as the median filter modifies an image by replacing each pixel value with the picture's neighborhood's median value [23]. This filter modifies an image in a nonlinear fashion. It does an excellent job of preventing the blurring of edges and details while also cutting down on noise. Figure 6 shows the median filtered result for the first 10 bands. In Table 1, the variations in data are compared between the original and filtered datasets for a subset of randomly selected bands, each corresponding to specific wavelengths.

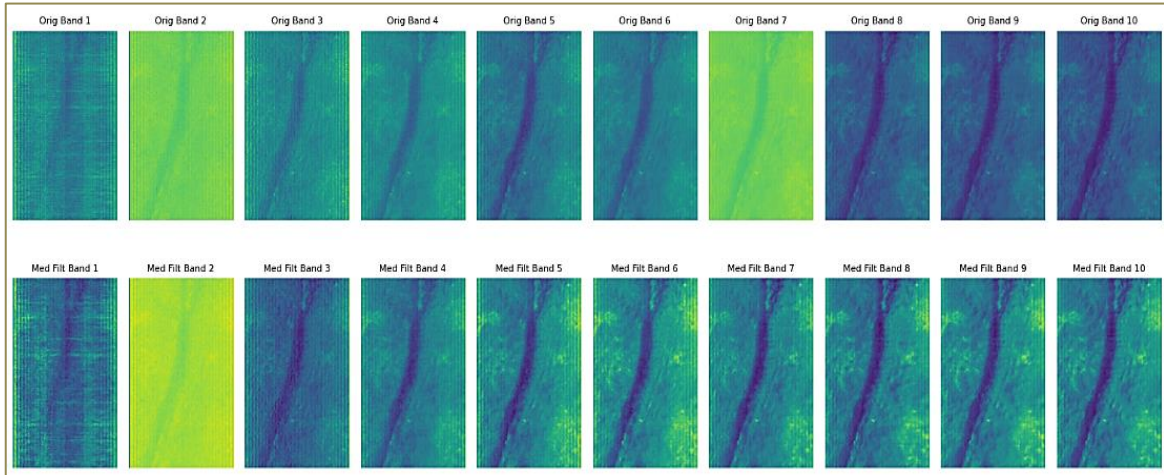


Figure 6. Median filtered band visualization: Band 1-10 (The top row depicts the original band and the bottom row depicts the median filtered band. Due to limitation of projecting all 198 band, only 10 band view has been laid)

Table 1. The different techniques applied with the variability in outcome and noise reduction

Technique	Advantages	Disadvantages	PSNR improvement	Applicability
Non-local means	Good for certain bands	Inconsistent across bands	Low to medium	Selected bands
Wavelet denoising	Effective in some contexts	Poor results on several bands	Low to medium	Selected bands
PCA	Reduces dimensionality, aids in noise reduction	Limited denoising impact alone	Medium	In combination with other techniques
MNF	Enhances signal-to-noise ratio	Not as effective for all bands	Medium	Selected scenarios
Denoising autoencoder	Superior denoising, adaptable to all bands	Requires significant computational resources	High (14 to 44 dB)	Comprehensive denoising

3.5. Statistical denoising techniques

We will use multiple statistical denoising approaches using median-filtered EO-1 HSI data to illustrate the best strategy for the region of interest. This compares how well different denoising approaches preserve vital information while lowering noise. The findings will determine the best hyperspectral image quality enhancement method for this scenario.

3.5.1. Non-local means

Non-local means (NLM) is especially beneficial for hyperspectral high-dimensional data such as high dynamic range (HDR) surface images [13]. For each pixel in the image, a tiny local patch is extracted (a small neighborhood surrounding the pixel). This approach allows for more accurate noise reduction and better preservation of image details by considering the similarity between patches rather than individual pixels.

Using a similarity metric such as the Euclidean distance between pixel values within the patches, the similarity between patches is calculated. Similar modifications to the target patch are distributed throughout the image. Similarity values are utilized to determine the weights for each of these similar regions. More comparable regions are assigned greater weights. The noisy pixel is then substituted with a weighted average of the pixel values in these similar regions, the weights of which are determined by the calculated similarities.

The aforementioned procedure is repeated for each pixel in the 198 bands of the image. From the output generated by applying NLM, it was apparent that the mean square error (MSE) values for the majority of bands are relatively low, which is desirable and indicates that the denoising method is effective at reducing noise for few bands, while for others the noise prevails. Nevertheless, the peak signal-to-noise ratio (PSNR) values vary across various bands, indicating that the denoising performance may be superior for certain bands, unlikely for others. Some bands are even observed to have negative PSNR values, which can occur when the noise in the denoised image is larger than the original image, perhaps as a result of excessive flattening. Figure 7 illustrates the first 10 denoised bands, revealing a relatively subtle visual impact of the denoising process.

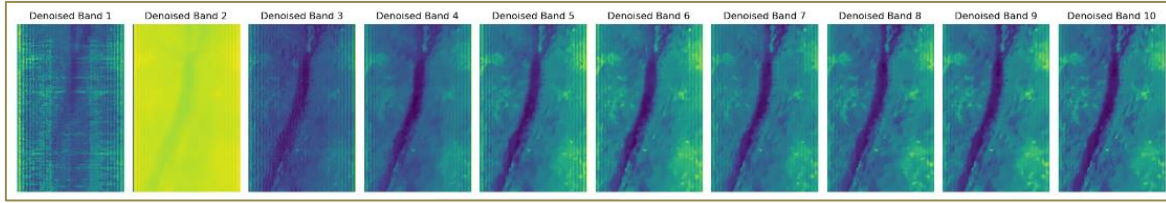


Figure 7. NLM denoised band visualization: Band 1-10 (due to limitation of projecting all 198-band result, only 10 band view has been laid)

3.5.2. Wavelet Denoising

This technique uses the mathematical concept of wavelets to decompose an image into multiple scales, separating noise from the underlying signal [14]. Haar wavelet transform-based wavelet denoising is applied to each band of median-filtered data. Figure 8 shows the first 10 denoised bands which in itself shows less visual denoising impact in comparison to even the NLM denoising method. Although a few bands were retrieved with effective denoising, other bands showed poor results. Noting that some bands have “nan” (not a number) values as observation for both MSE and PSNR is essential. This could be the result of division by zero or other mathematical faux pas during denoising.

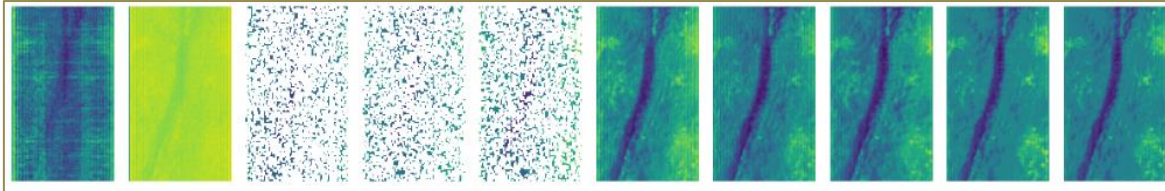


Figure 8. Wavelet denoising based band visualization (Denoised): Band 1-10 (Due to limitation of projecting all 198-band result, only 10 band view has been laid)

3.5.3. Principle component analysis for noise removal

Principal component analysis is a common technique for noise reduction in images, including median-filtered HDR images. PCA operates by transforming the data into a new coordinate system, where the first few principal components capture the most significant data variation [22]. By retaining only, the most important principal components, PCA can effectively reduce noise while preserving the essential features of the image [15].

Assume that the input image X has the dimensions $M \times N$, where M is the number of pixels in each row and N is the number of pixels in each column. If the image has B bands, then the size of X will be $M \times N \times B$. First, we transform the image into a data matrix D with dimensions $(M \times N) \times B$, where each row represents a pixel and its associated band values. We compute the mean vector of the data matrix D , where D is a $1 \times P$ vector.

In the mean centering phase, the mean vector is subtracted from each row of D to center the data around the origin. Next, we calculate the covariance matrix C of the mean-centered data. The covariance matrix measures the relationships between different bands (features) in the data.

$$C = (1/(M \times N)) \times D_{centered}^T \times D_{centered} \quad (2)$$

We next perform an eigen decomposition of the covariance matrix C . This involves finding the eigenvectors and eigenvalues of C .

$$C \times V = \lambda \times V \quad (3)$$

where V is a matrix containing the eigenvectors (principal components) as columns, and λ is a diagonal matrix containing the eigenvalues. The eigenvectors in V are ranked by their corresponding eigenvalues in λ . The first principal component with the highest eigenvalue captures the most significant variation in the data. Following eigenvectors capture a diminishing quantity of variation.

We can choose the top k eigenvectors to form a transformation matrix W with dimensions $P \times k$.

$$W = (v_1, v_2, \dots, v_k) \quad (4)$$

Finally, we perform dimensionality reduction by projecting the mean-centered data $D_{centered}$ onto the new coordinate system defined by the transformation matrix W . The resulting matrix $D_{reduced}$ has dimensions $(M \times N) \times k$, and it contains the reduced representations of each pixel in the image. We can now reconstruct the denoised image by applying the inverse transformation.

$$D_{denoised} = D_{reduced} \times W^T \quad (5)$$

Then, we add back the mean vector μ to get the denoised data matrix $D_{denoised}$.

$$denoised_image = D_{denoised} + \mu \quad (6)$$

The reduced representation $D_{reduced}$ contains the principal components that explain the most significant variations in the data. Figure 9 illustrates the original versus denoised band visualization. Figure 9(a) presents a 3D scatter plot comparing the original and denoised data, showing their overlap and highlighting minimal differences. Figure 9(b) depicts the spectral profile of PCA-denoised data across various wavelengths for 198 bands.

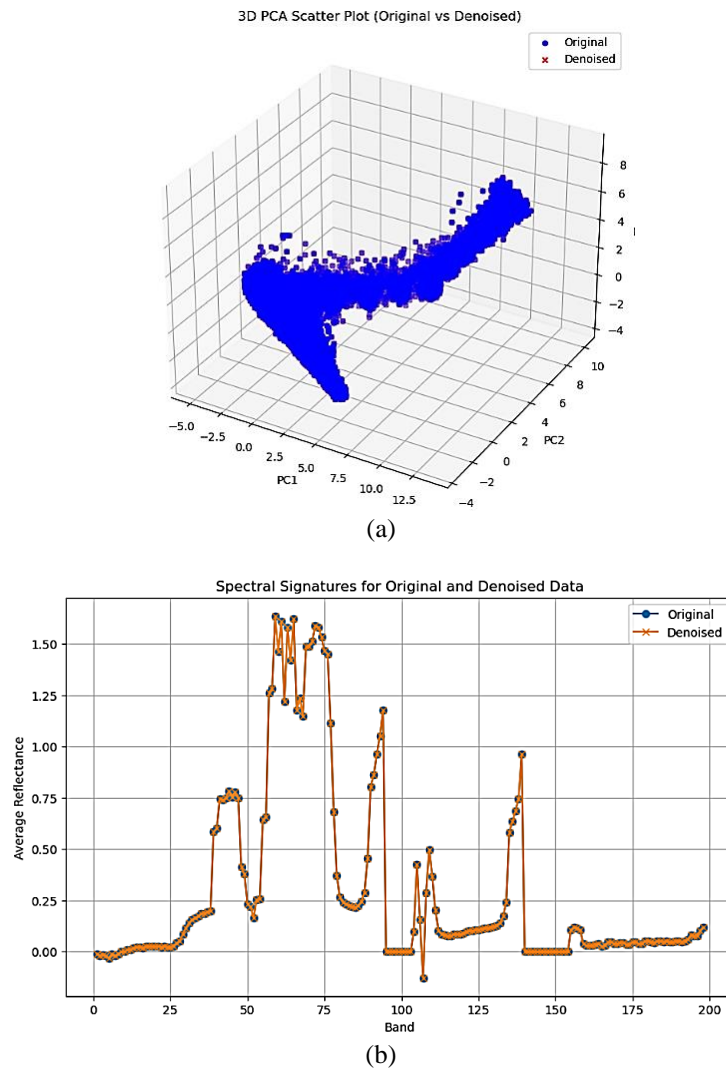


Figure 9. Original vs denoised band visualization (a) 3D Scatter plot view of original and denoised data and (b) Spectral profile of PCA denoised data over different wavelengths

By keeping only, a small number of principal components ($k \ll B$), we effectively reduce noise and remove irrelevant information from the image while retaining its essential features. The result however indicated that the denoising process has not resulted in a significant separation between the two datasets. Even after altering the PCA component no significant reduction was witnessed. Figure 7 indicate that the PCA technique standalone did not yield satisfactory. Figure 10 showcases the MSE and PSNR profile obtained by processing the bands applying standalone PCA technique.

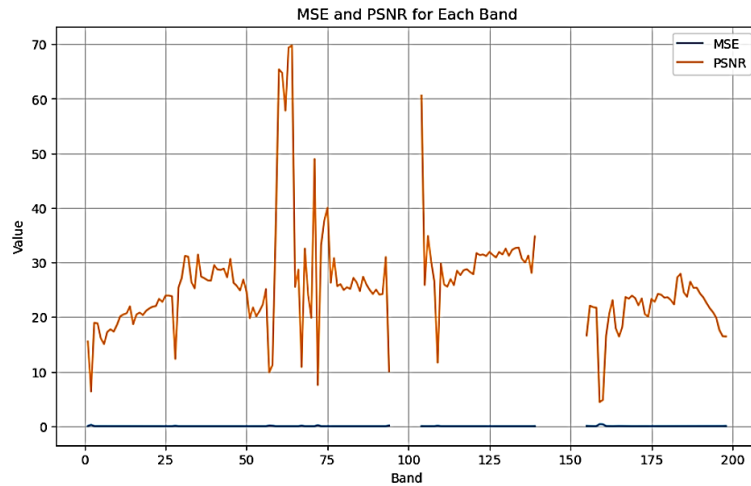


Figure 10. MSE and PSNR ratio for 198 bands processed with PCA

3.5.4. Minimum noise factor

Although PCA yields expected results in most of the cases, for our EO-1 HSI data, we did not get the satisfactory denoising. We will now employ MNF that complements PCA by addressing certain facets that PCA alone might not optimally manage. MNF when combined with PCA, can enhance the noise reduction process by emphasizing signal-capturing components and suppressing noise-representing components. MNF is a technique used for denoising and dimensionality reduction in remote sensing and image processing. It is particularly useful for enhancing the signal-to-noise ratio of multi/hyperspectral imagery [24].

MNF works by transforming the data into a new space where the first few components capture most of the signal variance while the last components capture noise. By discarding the components that represent noise, the data can be denoised. Figure 11 depicts the spectral profile of MNF denoising which was found to be better than PCA but still does not yield the expected denoising. Figure 12 shows the denoising results of MNF.

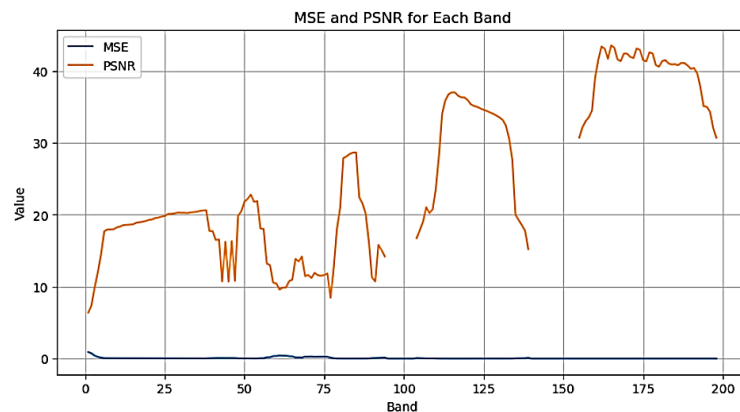


Figure 11. MSE and PSNR ratio for 198 bands processed with MNF (better results in comparison to standalone PCA)

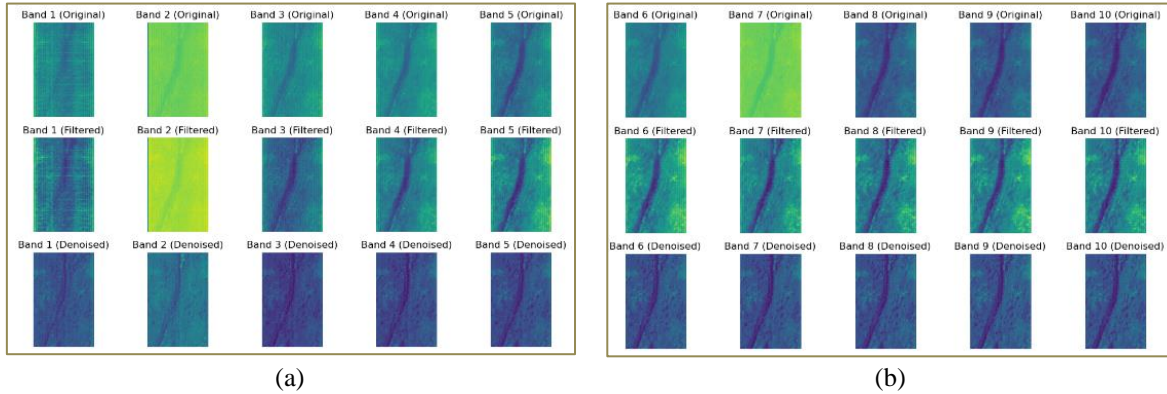


Figure 12. MNF denoising based band visualization: Band 1-10 (The top row depicts the original band, the medium row depicts median filtered data, and bottom row depicts the MNF filtered band. Due to limitation of projecting all 198 band, only 10 band view has been laid)

3.6. Machine learning based denoising

Even though we were able to denoise the 198 bands to a certain extent using statistical methods, we observed inconsistencies and anomalies in a great number of bands. To improve the quality of the data, we employed the median-filtered EO-1 HSI data with 198 bands as the foundation for further processing. Moving forward, we will implement machine learning-based denoising technique to address the unique challenges of the region of interest, enhancing the overall accuracy and reliability of the results.

3.6.1. Denoising autoencoder

A denoising autoencoder is a neural network architecture commonly employed to denoise data, encompassing high-dimensional datasets such as HDR hyperspectral images. Autoencoders have demonstrated their efficacy in successfully eliminating random noise that may be created during the process of image recuperation or broadcast. Autoencoders have the potential to mitigate diverse visual artefacts, contingent upon their specific architecture and training methodology.

Autoencoders are a category of machine learning algorithms that fall under the unsupervised learning paradigm. This implies that they possess the capability to learn patterns and structures in data without the need for labelled examples during the training process [25], [26]. Individuals have the capacity to acquire the skills necessary to effectively represent and reconstruct input data through the acquisition of knowledge in efficient data compression and decompression methods. To denoise the EO-1 HDR HSI dataset, we have followed the flow of steps depicted in Figure 13.

Denoising autoencoder (DAE) is trained to map erratic input data to clear and denoised representations. It has two major components: an encoder and a decoder. The encoder compresses the noisy HDR hyperspectral image into a lower-dimensional latent representation. Typically, the encoder network comprises multiple layers of neurons, with each layer deriving higher-level features from the input data. The final layer of the encoder generates the compressed representation, which is a bottleneck and has smaller dimensions than the original image. The decoder reconstructs the denoised HDR hyperspectral image from the encoder's compressed representation (latent space). The decoder consists of multiple layers, but in the opposite order as the encoder. The final layer of the decoder outputs the denoised image, which approximates the original pure image as closely as possible [27].

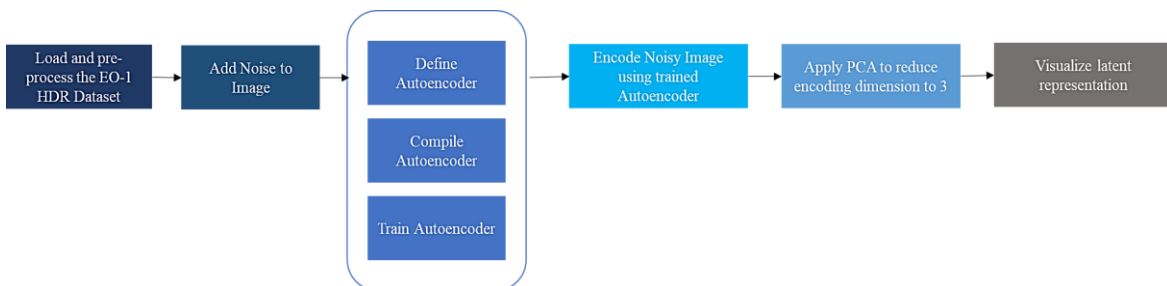


Figure 13. Denoising autoencoder denoising approach applied to EO-1 Hyperion dataset

During training, pairings of noisy HDR hyperspectral images and their clear counterparts are transmitted to the autoencoder. However, we add random noise to the clear images before using them for training. The noisy images serve as inputs, while the clear images function as ground truth targets. Figure 10 depicts the denoising autoencoder mechanism applied to Band 1 of 198 HIS bands. The process is iteratively applied to each band to get reconstructed denoised image. PCA is effectively employed in the latent space code construct. The autoencoder's objective is to minimize the difference between the denoised outputs and the corresponding clean images.

The training process involves the following steps:

- Feed a noisy HDR hyperspectral image to the encoder (*Add pre-processed data plus add noise*)
- The encoder compresses the noisy image into a lower-dimensional representation (latent space).
- The decoder then takes this compressed representation and reconstructs the denoised image.
- Compare the denoised image with the corresponding clean image and compute the reconstruction loss (typically using mean squared error or binary cross-entropy loss).
- Backpropagate the reconstruction loss through the network and update the model's weights using an optimization algorithm (Adam optimizer) `autoencoder.compile(optimizer = 'adam', loss = 'binary_crossentropy')`.
- Repeat steps 1 to 5 for a batch of noisy images and their corresponding clean images.
- Iterate through multiple epochs, updating the model's weights with each iteration, until the loss converges or reaches a satisfactory level. (Refer Figure 14 for the flow of process).

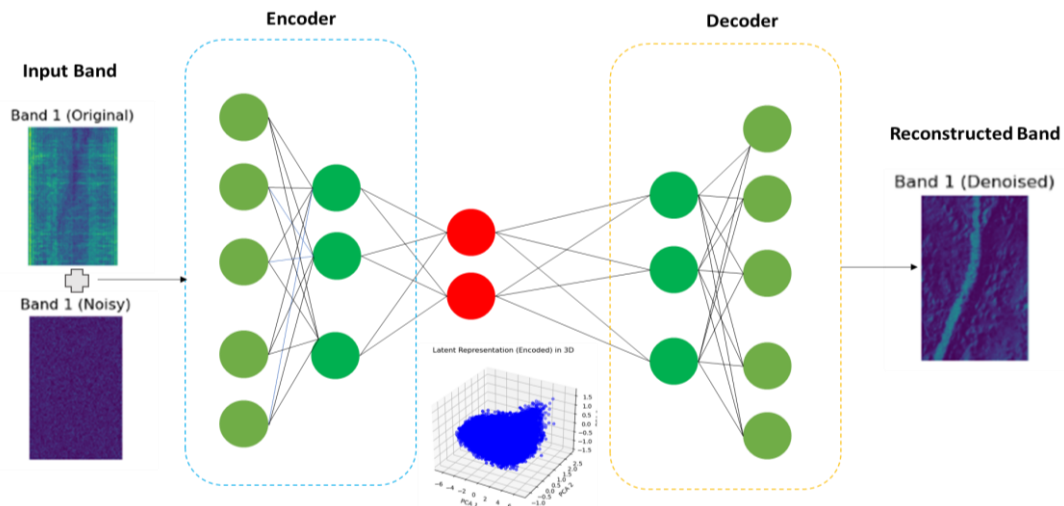


Figure 14. Denoising autoencoder based denoising applied on Band 1 replicated to all 198 bands

In the employed algorithm for the denoising autoencoder, two activation functions are applied: rectified linear unit (ReLU) and 'sigmoid'. The ReLU activation function is used in the encoding layer of the autoencoder.

$$\text{encoded} = \text{tf.keras.layers.Dense}(\text{encoding_dim}, \text{activation} = \text{'relu'})(\text{input_image}) \quad (7)$$

ReLU facilitates quicker learning and can result in sparse activations, which can be desirable in certain circumstances. The Sigmoid activation function is used in the decoding layer of the autoencoder:

$$\text{decoded} = \text{tf.keras.layers.Dense}(\text{input_shape}[-1], \text{activation} = \text{'sigmoid'})(\text{encoded}) \quad (8)$$

Once trained, the denoising autoencoder can effectively denoise new noisy HDR hyperspectral images. The denoising autoencoder is a potent technique for noise removal in high-dimensional data, such as hyperspectral images, because it learns meaningful representations in the compressed latent space, effectively filtering out undesirable noise and preserving essential features in the denoised output. Denoising autoencoder produced the greatest denoising results among all techniques utilized. Figure 15 depicts the denoising autoencoder based band 1-10 visualization.

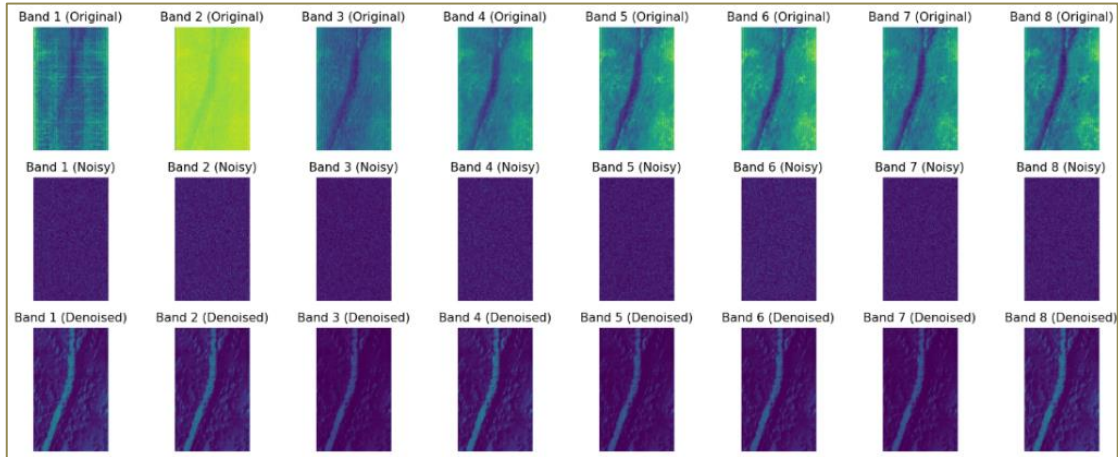


Figure 15. Denoising autoencoder based band visualization: Band 1-10 (The top row depicts the original band, the medium row depicts added noise, and bottom row depicts the denoised data employing autoencoders. Due to limitation of projecting all 198 band, only 10 band view has been laid)

A crucial aspect of training machine learning models, including autoencoders, is determining the number of training epochs and sample size. The selection of these hyperparameters can have a substantial effect on the training procedure and the resultant model performance. Here's how we ascertained the appropriate parameter values:

- Start with a moderate number of epochs, such as 50 or 100, to evaluate the performance of the model at the outset. For our work 50 epochs yielded satisfactory results
- For efficient computation on graphics processing unit (GPUs), we have selected the batch size of 128.
- During training, we tracked the training loss and validation loss. If the validation loss ceases to decrease or begins to increase, the model may be overfit. You can discontinue training or employ techniques such as early ceasing. Figure 16 shows the decreasing loss values.
- We started with 100 epochs which observably showed overfitting.
- Determined the optimal sample size to strike a balance between training speed and model performance through experimentation. Larger group sizes may necessitate additional epochs for appropriate convergence.

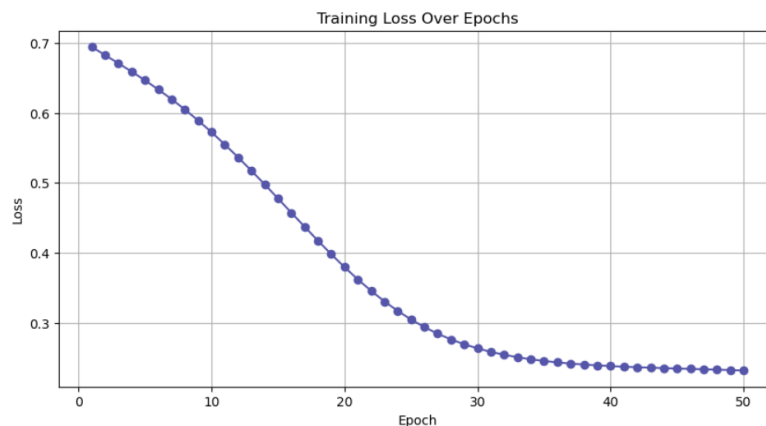


Figure 16. Decreasing loss value with epochs 1-50

As training progresses, the autoencoder learns to extract meaningful features from the input data, effectively denoising it by reconstructing the original information. The decrease in loss indicates that the autoencoder is becoming more effective at achieving this objective. For the denoising autoencoder applied to our EO-1 HSI dataset, the peak signal-to-noise ratio (PSNR) increases from 14 to 44 dB, indicating an enhancement in image quality. The progression obtained demonstrates a range of effective PSNR values beginning at 14 dB and progressively increasing to 44 dB. This range represents the enhancement in image

quality brought about by the denoising process. A PSNR of 14 dB indicates that the signal-to-noise ratio is relatively low, signifying that the noise level is substantial in comparison to the signal. As the PSNR increases, the denoising process becomes more efficient, reducing image noise and improving its quality. A PSNR of 44 dB indicates that the noise has been significantly reduced, and the denoised image closely resembles the original, noise-free image. Figure 17 shows the PSNR progression for our model over the cycle which depicts effects denoising being achieved, wherein Figure 17(a) shows the PSNR progression for the EO-1 HSI dataset across 198 bands, and Figure 17(b) shows the progression for selected bands (1,6,11,16).

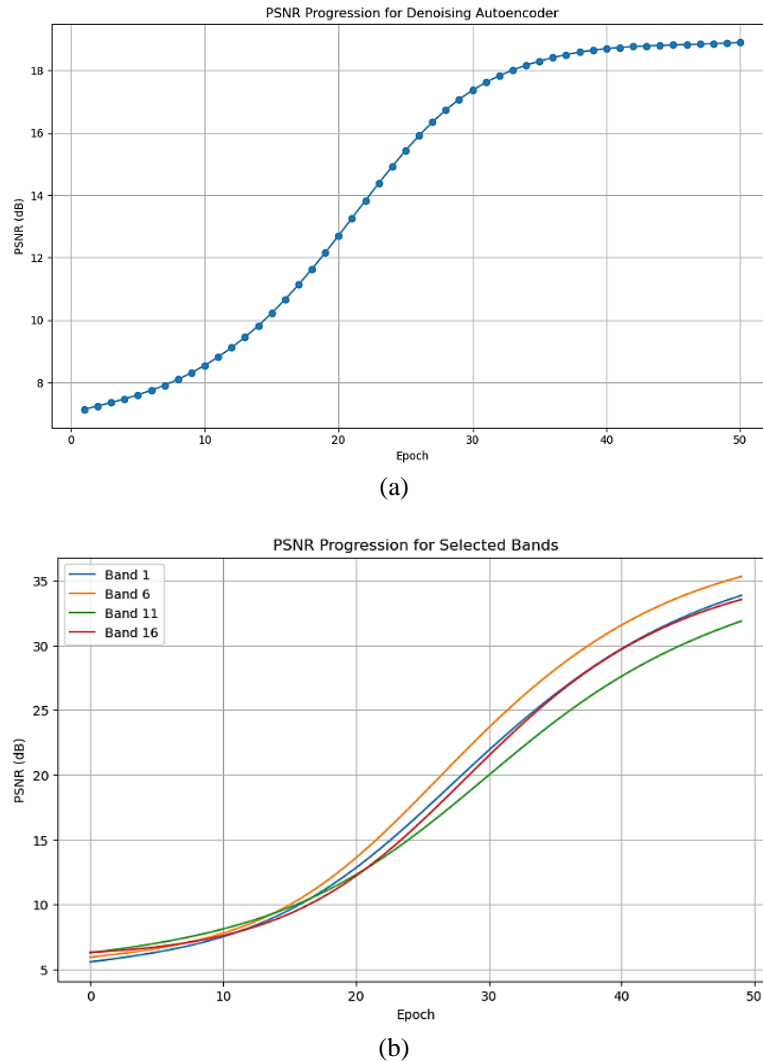


Figure 17. PSNR progression of denoising autoencoder (a) PSNR progression for the EO-1 HSI dataset and (b) PSNR Progression for selected bands (1,6,11,16)

4. RESULT

Our comprehensive analysis evaluated the efficiency of various denoising methods, including statistical denoising techniques (NLM, wavelet denoising, PCA, MNF), and a machine learning-based technique (denoising autoencoder), across 198 spectral bands of Hyperion EO-1 sensor data. The DAE demonstrated superior performance in noise reduction, significantly enhancing the PSNR from 14 to 44 dB, indicative of substantial improvements in data quality and fidelity. This is in contrast to the mixed results observed with traditional statistical methods, where techniques like NLM, wavelet denoising, and MNF showed satisfactory denoising for some bands but were ineffective for others. PCA, while having limited impact when used alone, contributed to enhanced outcomes when integrated with other methods or within the DAE framework.

5. DISCUSSION

The denoising autoencoder's efficacy underscores the potential of deep learning algorithms in processing hyperspectral imagery, offering substantial improvements over traditional statistical techniques. This aligns with the emerging trend of leveraging machine learning for remote sensing applications, acknowledging its ability to handle high-dimensional data and complex noise structures. The varied performance of statistical techniques across different bands highlights the challenge in applying a one-size-fits-all approach to hyperspectral denoising. While these methods have their merits, particularly in specific contexts or as part of a hybrid approach, the adaptive nature of machine learning models, exemplified by the denoising autoencoder, presents a more robust solution to the intricate problem of hyperspectral image denoising. Table 1 summarizes the different technique employed for the EO-1 dataset with the outcome achieved for effective noise reduction

6. CONCLUSION

In this study, we investigated the crucial task of denoising hyperspectral data to improve the accuracy of mineral mapping. Multiple bands and iterations of data were used to evaluate various denoising techniques, including both traditional statistical approaches and modern machine learning methods. Our analysis reveals the efficacy of nuanced denoising, illuminating the limitations and strengths of each method. The final objective was to prepare the denoised dataset for subsequent endmember extraction, spectral unmixing, and exhaustive mineral mapping in the Kiriburu Region. Our analysis demonstrates the variable performance of traditional denoising methods across different bands. While methods like NLM, wavelet denoising, and MNF exhibit satisfactory denoising for certain bands, they faltered for others. PCA by itself had limited denoising effects. Nonetheless, when combined with statistical techniques such as MNF or incorporated into the architecture of denoising autoencoders using a machine learning approach, it contributed to more pronounced denoising effects. Our unsupervised machine learning method yielded remarkable results, demonstrating a significant improvement in PSNR and proving its effectiveness. Effective denoising arises as a crucial preliminary stage in the pursuit of accurate mineral mapping through hyperspectral data. Our research not only emphasizes the diverse performance of denoising techniques across spectral bands, but also the transformative potential of machine learning integration. This work not only contributes to the field of remote sensing, but it also provides a comprehensive instruction in the nuanced art of data preprocessing. The work serves as preparatory work towards mineral prospectivity mapping.




REFERENCES

- [1] N. Rani, "Application of remote sensing techniques in geological mapping and mineral exploration - a case study from Dharwar Craton," *Journal of the Geological Society of India*, vol. 98, no. 1, pp. 144–145, Jan. 2022, doi: 10.1007/s12594-022-1943-z.
- [2] M. G. Tagwai, O. A. Jimoh, S. A. Shehu, and H. Zabidi, "Application of GIS and remote sensing in mineral exploration: current and future perspectives," *World Journal of Engineering*, vol. 21, no. 3, pp. 487–502, Mar. 2024, doi: 10.1108/WJE-09-2022-0395.
- [3] B. Lu, P. D. Dao, J. Liu, Y. He, and J. Shang, "Recent advances of hyperspectral imaging technology and applications in agriculture," *Remote Sensing*, vol. 12, no. 16, Aug. 2020, doi: 10.3390/RS12162659.
- [4] Q. Du and H. Yang, "Unsupervised band selection for hyperspectral image analysis," in *International Geoscience and Remote Sensing Symposium (IGARSS)*, 2007, pp. 282–285. doi: 10.1109/IGARSS.2007.4422785.
- [5] M. Akewar and M. Chandak, "Hyperspectral imaging algorithms and applications: a review," *Authorea Preprints*, Jan. 2023, doi: 10.36227/techrxiv.24743562.v2.
- [6] G. Nguyen *et al.*, "Machine learning and deep learning frameworks and libraries for large-scale data mining: a survey," *Artificial Intelligence Review*, vol. 52, no. 1, pp. 77–124, 2019, doi: 10.1007/s10462-018-09679-z.
- [7] W. Huang, Z. Zhao, L. Sun, and M. Ju, "Dual-branch attention-assisted CNN for hyperspectral image classification," *Remote Sensing*, vol. 14, no. 23, p. 6158, Dec. 2022, doi: 10.3390/rs14236158.
- [8] X. Lian *et al.*, "A neural network for hyperspectral image denoising by combining spatial-spectral information," *Remote Sensing*, vol. 15, no. 21, Oct. 2023, doi: 10.3390/rs15215174.
- [9] R. H. Chan and R. Li, "A 3-stage spectral-spatial method for hyperspectral image classification," *Remote Sensing*, vol. 14, no. 16, Aug. 2022, doi: 10.3390/rs14163998.
- [10] X. Feng, L. He, Q. Cheng, X. Long, and Y. Yuan, "Hyperspectral and multispectral remote sensing image fusion based on endmember spatial information," *Remote Sensing*, vol. 12, no. 6, Mar. 2020, doi: 10.3390/rs12061009.
- [11] C. Zhu *et al.*, "Hyperspectral and multispectral remote sensing image fusion using SwinGAN with joint adaptive spatial-spectral gradient loss function," *International Journal of Digital Earth*, vol. 16, no. 1, pp. 3580–3600, Sep. 2023, doi: 10.1080/17538947.2023.2253206.
- [12] S. Zhao *et al.*, "A hyperspectral image denoising method based on land cover spectral autocorrelation," *International Journal of Applied Earth Observation and Geoinformation*, vol. 123, Sep. 2023, doi: 10.1016/j.jag.2023.103481.
- [13] C. Deng, L. Li, Z. He, J. Li, and Y. Zhu, "Monte Carlo non-local means method for hyperspectral image denoising," in *International Geoscience and Remote Sensing Symposium (IGARSS)*, Jul. 2018, pp. 4772–4775. doi: 10.1109/IGARSS.2018.8519108.
- [14] H. Yang *et al.*, "Application and evaluation of wavelet-based denoising method in hyperspectral imagery data," in *IFIP Advances in Information and Communication Technology*, vol. 369, Springer Berlin Heidelberg, 2012, pp. 461–469. doi: 10.1007/978-3-642-27278-3_47.
- [15] S. Xiaorui and W. Lingda, "Denoising of hyperspectral images based on principal component analysis and adaptive sparse




- coding,” in *2018 10th IAPR Workshop on Pattern Recognition in Remote Sensing (PRRS)*, Aug. 2018, pp. 1–6. doi: 10.1109/PRRS.2018.8486272.
- [16] J. Granek, “Application of machine learning algorithms to mineral prospectivity mapping,” Ph.D. thesis, University of British Columbia, 2016.
- [17] S. Wang, K. Zhou, J. Wang, and J. Zhao, “Identifying and mapping alteration minerals using HySpex airborne hyperspectral data and random forest algorithm,” *Frontiers in Earth Science*, vol. 10, Jun. 2022, doi: 10.3389/feart.2022.871529.
- [18] USGS, “U.S. geological survey global visualization viewer, ‘EarthExplorer,’” *USGS Global Visualization Viewer (GloVis)*. 2024. <https://glovis.usgs.gov> (accessed Mar 6, 2024).
- [19] H. Fu *et al.*, “A novel band selection and spatial noise reduction method for hyperspectral image classification,” *IEEE Transactions on Geoscience and Remote Sensing*, vol. 60, pp. 1–13, 2022, doi: 10.1109/TGRS.2022.3189015.
- [20] L. Wang, X. Jia, and Y. Zhang, “A novel geometry-based feature-selection technique for hyperspectral imagery,” *IEEE Geoscience and Remote Sensing Letters*, vol. 4, no. 1, pp. 171–175, Jan. 2007, doi: 10.1109/LGRS.2006.887142.
- [21] Q. Qin, Z. Zhang, L. Chen, N. Wang, and C. Zhang, “Oil and gas reservoir exploration based on hyperspectral remote sensing and super-low-frequency electromagnetic detection,” *Journal of Applied Remote Sensing*, vol. 10, no. 1, p. 16017, Feb. 2016, doi: 10.1117/1.jrs.10.016017.
- [22] H. Zhang, J. Cai, W. He, H. Shen, and L. Zhang, “Double low-rank matrix decomposition for hyperspectral image denoising and destriping,” *IEEE Transactions on Geoscience and Remote Sensing*, vol. 60, pp. 1–19, 2022, doi: 10.1109/TGRS.2021.3061148.
- [23] B. Rasti, P. Scheunders, P. Ghamisi, G. Licciardi, and J. Chanussot, “Noise reduction in hyperspectral imagery: overview and application,” *Remote Sensing*, vol. 10, no. 3, p. 482, Mar. 2018, doi: 10.3390/rs10030482.
- [24] G. Luo, G. Chen, L. Tian, K. Qin, and S. E. Qian, “Minimum noise fraction versus principal component analysis as a preprocessing step for hyperspectral imagery denoising,” *Canadian Journal of Remote Sensing*, vol. 42, no. 2, pp. 106–116, Mar. 2016, doi: 10.1080/07038992.2016.1160772.
- [25] R. Lan, Z. Li, Z. Liu, T. Gu, and X. Luo, “Hyperspectral image classification using k-sparse denoising autoencoder and spectral-restricted spatial characteristics,” *Applied Soft Computing Journal*, vol. 74, pp. 693–708, Jan. 2019, doi: 10.1016/j.asoc.2018.08.049.
- [26] E. Kalinicheva, J. Sublime, and M. Trocan, “Neural network autoencoder for change detection in satellite image time series,” in *2018 25th IEEE International Conference on Electronics Circuits and Systems, ICECS 2018*, Dec. 2018, pp. 641–642. doi: 10.1109/ICECS.2018.8617850.
- [27] P. Li, Y. Pei, and J. Li, “A comprehensive survey on design and application of autoencoder in deep learning,” *Applied Soft Computing*, vol. 138, May 2023, doi: 10.1016/j.asoc.2023.110176.

BIOGRAPHIES OF AUTHORS






Priyanka Nair    with a distinguished blend of over a decade's experience spanning both the industry and academia, she has carved a niche in the rapidly evolving field of data science. Graduating with a B.E. in computer science and engineering from the prestigious Birla Institute of Technology, Mesra in 2012, and furthering her academic credentials with an M.Tech. from Manipal University Jaipur in 2017, she is actively contributing to technological realm as a profession. Currently, she holds the position of associate manager at Tredence Inc., with the role aligned to the domain of data science. In parallel to her professional pursuits, she is a dedicated Ph.D. scholar at Manipal University Jaipur, where her research is aligned to advanced machine learning applications within geosciences and remote sensing. Her research interests span a broad spectrum, including artificial intelligence, machine learning, data science, image processing, and data analytics. She can be contacted at priyankanair@live.com.



Devesh Kumar Srivastava    has been working in the capacity of professor (Sen. level) at Department of Information Technology, Manipal University Jaipur, Jaipur Rajasthan India since 2012. He has a total of 22 years rich experience of academic, research and administration activities. His research areas are software engineering, ML, DL. He is a professional member of IEEE and senior member of ACM. He chaired 42 technical sessions and addressed 12 keynote/invited talks in the international conferences of IEEE, Elsevier, ACM, and Springer. He published more than 100 articles in the journal and conference proceedings. He supervised 5 Ph.D. scholars. He can be contacted at email: devesh988@yahoo.com.



Roheet Bhatnagar    works at Manipal University Jaipur (MUJ as a full-time professor in the Department of CSE and has been associated with the Manipal group since June 2008. He has additional responsibility as director of research. He has vast experience spanning around 25 years both in industry as well as academics. He has done his B.E. in computer science, M.Tech. in remote sensing from Birla Inst. of Tech., Mesra, Ranchi. His Ph.D. is in engineering and in the software engineering domain from Sikkim Manipal Institute of Technology (SMIT), He is a senior member - IEEE, life members ISTE, ISRS and has published over 80 research papers in reputed conferences and journals. He can be contacted at email: roheet.bhatnagar@jaipur.manipal.edu.